The Seismic Record
A journal of the Seismological Society of America

Curved Fault Slip Captured by CCTV Video During the 2025 M_w 7.7 Myanmar Earthquake

OPEN ACCESS

Jesse Kearse*[1] and Yoshihiro Kaneko[1]

Abstract

On-fault geological observations from surface-breaking earthquakes typically contain curved slickenlines, suggesting fault slip is curved. However, slickenlines commonly record only a fraction of coseismic slip, making it difficult to reconstruct the full slip trajectory. Near-fault seismic records, though capable of capturing ground motions associated with rupture, are limited in their ability to constrain on-fault slip direction because they record motion on only one side of the fault. Here, we overcome these challenges by directly observing fault slip using video footage of the 2025 M_w 7.7 Myanmar, strike-slip earthquake. We use pixel cross correlation to track features in successive frames of the video, revealing a pulse of fault slip with a magnitude of 2.5 ± 0.5 m, a duration of 1.3 ± 0.2 s, and a peak velocity of 3.2 ± 1.0 m/s. The observed trajectory is notably curved and includes a transient (0.3 m) dip-slip component on a steeply dipping strike-slip fault. These observations are consistent with geological records of curved slickenlines, supporting mechanical models that link rupture propagation direction to near-surface slip curvature. Our results provide the first direct visual evidence of curved coseismic fault slip, bridging a critical gap among seismological observations, geological data, and theoretical models.

Cite this article as Kearse, J. and Y. Kaneko (2025). Curved Fault Slip Captured by CCTV Video During the 2025 M_w 7.7 Myanmar Earthquake, *The Seismic Record*. **5**(**3**), 281–288, doi: 10.1785/0320250024.

Supplemental Material

Introduction

Resolving the dynamics of fault slip during large earthquake ruptures is a major challenge in earthquake science. On-fault geological data represent a valuable archive of slip in surface-breaking earthquakes, recorded as slickenlines embedded into the fault plane itself (Spudich *et al.*, 1998; Kearse *et al.*, 2019; Barth *et al.*, 2024). Slickenlines are typically curved (Kearse and Kaneko, 2020), suggesting fault motions evolve dynamically during seismic slip. However, inferring the full coseismic slip trajectory from slickenlines is challenging because they typically record only a fraction of slip, or they may form a complex network of overlapping striations (Kearse and Kaneko, 2020; Little *et al.*, 2025). Because these observations are typically made days after the event, there is inherent uncertainty about the influence of nonseismic sources of slickenline formation, such as postseismic slip, or gravity-driven movement within the unstable ground surface rupture zone, limiting their potential to capture the dynamics of seismic slip.

Another approach to resolving the rate and direction of slip during earthquake rupture involves using near-field instrumental records—such as strong-motion seismometers or high-rate Global Navigation Satellite Systems—because ground motions within a few kilometers of the fault are dominated by the direct effects of fault slip (the so-called near-field terms; Bouchon *et al.*, 2000; Kearse *et al.*, 2024). However, because of their off-fault location, it is unclear to what extent these records are contaminated by free-surface effects and whether they are able to resolve the cohesive zone of the propagating rupture (Cruz-Atienza *et al.*, 2009). Furthermore, because instruments are typically located on only one side

1. Department of Geophysics, Graduate School of Science, Kyoto University, Kyoto, Japan, https://orcid.org/0000-0003-1223-2549 (JK); https://orcid.org/0000-0003-2342-0131 (YK)

*Corresponding author: jesse@kearse.co.nz

of the fault, reconstructing the relative motion between both sides is not straightforward.

In this article, we overcome these challenges using closed-circuit television (CCTV) video footage of ground surface rupture during the 2025 moment magnitude (M_w) 7.7 Myanmar, earthquake, which provides the first direct observation of surface fault slip in real time. We track objects by pixel cross correlation in successive frames of the video to measure the rate and direction of fault motion during coseismic slip. Our observations show that slip near the ground surface is distinctly curved. We demonstrate that these new observations are consistent with previous reports of curved slickenlines and recent models of dynamic rupture propagation, and we discuss how these data provide an important link between physics-based earthquake simulations, on-fault geological data, and near-fault observations of strong ground motion.

Video Analysis of the Myanmar Earthquake

The 2025 M_w 7.7 Myanmar earthquake occurred on 28 March, with a hypocenter 20 km west of Mandalay city, Myanmar, at a depth 10 km (U.S. Geological Survey [USGS], 2025). The hypocenter location and right-lateral strike-slip mechanism are consistent with rupture on the Sagaing fault, a major north-striking structure accommodating right-lateral shear between the Burma plate to the west and Sundaland to the east (Vigny *et al.*, 2003). The earthquake lasted ~90 s (Inoue *et al.*, 2025) and propagated both north and south, with total a rupture length exceeding 400 km and surface strike slip exceeding 6 m (Fig. 1). Because of the exceptionally long rupture, strong ground shaking of modified Mercalli intensity X (10) extended over a broad area, causing widespread damage to homes, sites of historical and cultural significance, and key infrastructure in Myanmar, resulting in 3600 confirmed fatalities (Witze, 2025).

At the time of the earthquake, a CCTV security camera was recording video at the trace of the Sagaing fault, 120 km south of earthquake hypocenter (Fig. 1). The camera was positioned ~20 m to the east of the Sagaing fault and was facing southwest across the fault (Fig. 1b,c). The remarkable footage clearly shows relative northward translation of the western side of the fault during coseismic slip on the Sagaing fault, which lasted ~2 s and was accompanied by the simultaneous formation of a 1–2 m wide mole track along the surface rupture trace.

We use a windowed pixel cross-correlation approach to measure the accrual of slip across the Sagaing fault from the first frame of the video (Fig. 2a) to the last frame (Fig. 2b). To track displacements on the west side of the fault, we define 25 overlapping 26 × 26 pixel subsets of the image each containing objects located 70–80 m from the camera. Our analysis is based primarily on the subset that produced the sharpest cross correlation results ("target," Fig. 2a); however, our results are consistent across all subsets analyzed. We also track features on the eastern side of the fault, the same side as the camera (e.g., "noise," Fig. 2a).

Figure 2c shows the displacement time series of tracked features relative to the image frame over the duration of the video. Ground shaking commences at 9.5 ± 0.1 s, characterized by coherent motion of both features (target and noise), and is followed by stronger shaking at 12 ± 0.1 s. The displacement time series of the target begins to diverge from the noise at 14.1 ± 0.1 s ~5 s after the first arrivals. Later at 15.4 ± 0.1 s, both features resume their coherent, time-synchronized displacements, which continue until the last frame of the record. During this 1.3 s interval, the largest pixel displacements are observed for the target: +33 pixels in the positive x direction and −13 pixels in the negative y direction. In contrast, the feature on the near side of the fault shows relatively minor displacements: −1 pixel in x and −7 pixels in y.

To estimate the time series of slip across the Sagaing fault, we follow a workflow to convert from pixel displacement to meters on the Sagaing fault plane (Fig. S1, available in the supplemental material to this article). First, we subtract the displacement time series of the noise from the target (Fig. 2c). This removes noise introduced by wobbling and tilting of the camera during ground shaking. Next, we use fence posts of known spacing and orientation (while accounting for lens distortion and parallax) to estimate displacements in units of meters at the target location (Figs. S3 and S4). By projecting the displacements along the fault parallel direction estimated from postearthquake satellite imagery, we obtain the strike-slip and dip-slip components of relative fault motion (Fig. S6). To obtain the slip velocity function, we differentiate the displacement time series and apply a 0.2 s moving average to suppress artifacts introduced by the discrete digital sampling (24 frames/second). Uncertainties in the measured pixel displacements are calculated at each frame from the sharpness of the 2D cross-correlation function (Fig. S2) and are carried forward into uncertainties in fault slip using the same workflow.

Coseismic Slip of the Sagaing Fault

Our analysis reveals coseismic slip across the Sagaing fault as a smooth ramp-like slip function with an amplitude of 2.5 ± 0.5 m and a duration of 1.3 ± 0.2 s (Fig. 2d). Down-to-the-west

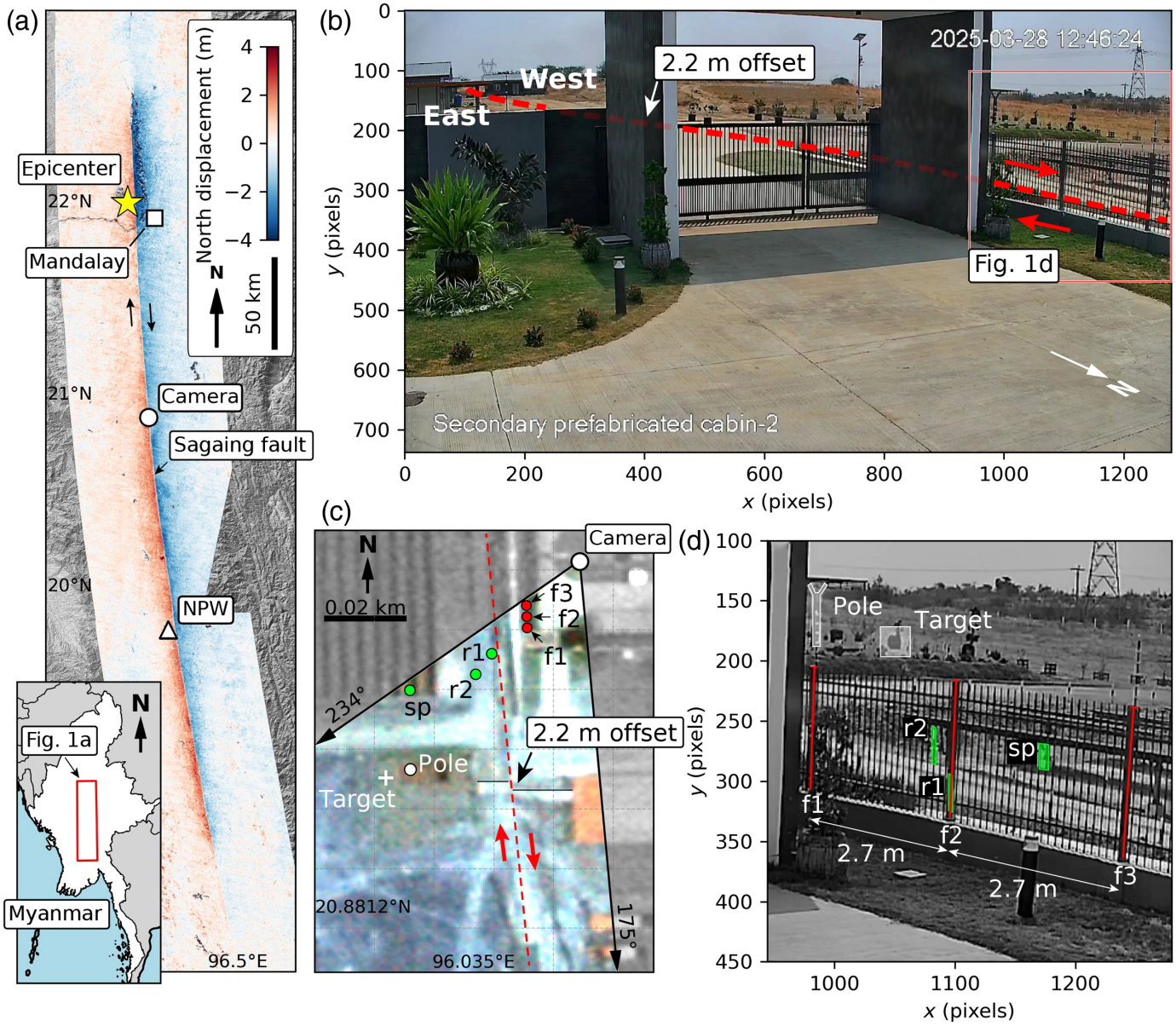

Figure 1. (a) Map of Myanmar (inset) and the Myanmar earthquake. Red and blue colors show the coseismic surface displacement field derived from sentinel-2 images taken before and after, the earthquake from Van Wyk De Vries (2025). The locations of the CCTV camera and strong-motion station NPW are shown. (b) Frame 1 of video (before rupture arrives) showing the field of view captured by the CCTV camera. The red dashed line shows the location of the Sagaing fault rupture. The offset path is obscured behind the gate structure in the foreground. (c) Planet labs satellite image with a 0.5 m resolution taken after the earthquake (5 April 2025). Features observable in panel (d) are labeled. The colorized area corresponds to the field of view of the video frame in panel (b). f1–f3 denote fence posts located on the east side of the fault used to calibrate coseismic displacements. r1, r2, sp, and pole are objects that are displaced by fault motion. The white cross labeled "target" shows the location of features tracked using image cross correlation. (d) Enlarged subset of the video frame showing the locations of the objects in pixel coordinates.

dip-slip displacement reaches a maximum of 0.3 ± 0.25 m only 0.5 s after the onset of slip, subsequently reducing to 0.2 ± 0.25 m. The magnitude of net slip agrees well with the postearthquake satellite observation of a discrete footpath offset of 2.2 ± 0.5 m (e.g., Fig. 1c). We calculated additional displacements of 2.2 ± 0.5, 2.2 ± 0.5, and 2.3 ± 0.5 m for three objects located on the western side of the Sagaing fault at distances of 5, 10, and 35 m from the fault trace, respectively (r1, r2, sp,

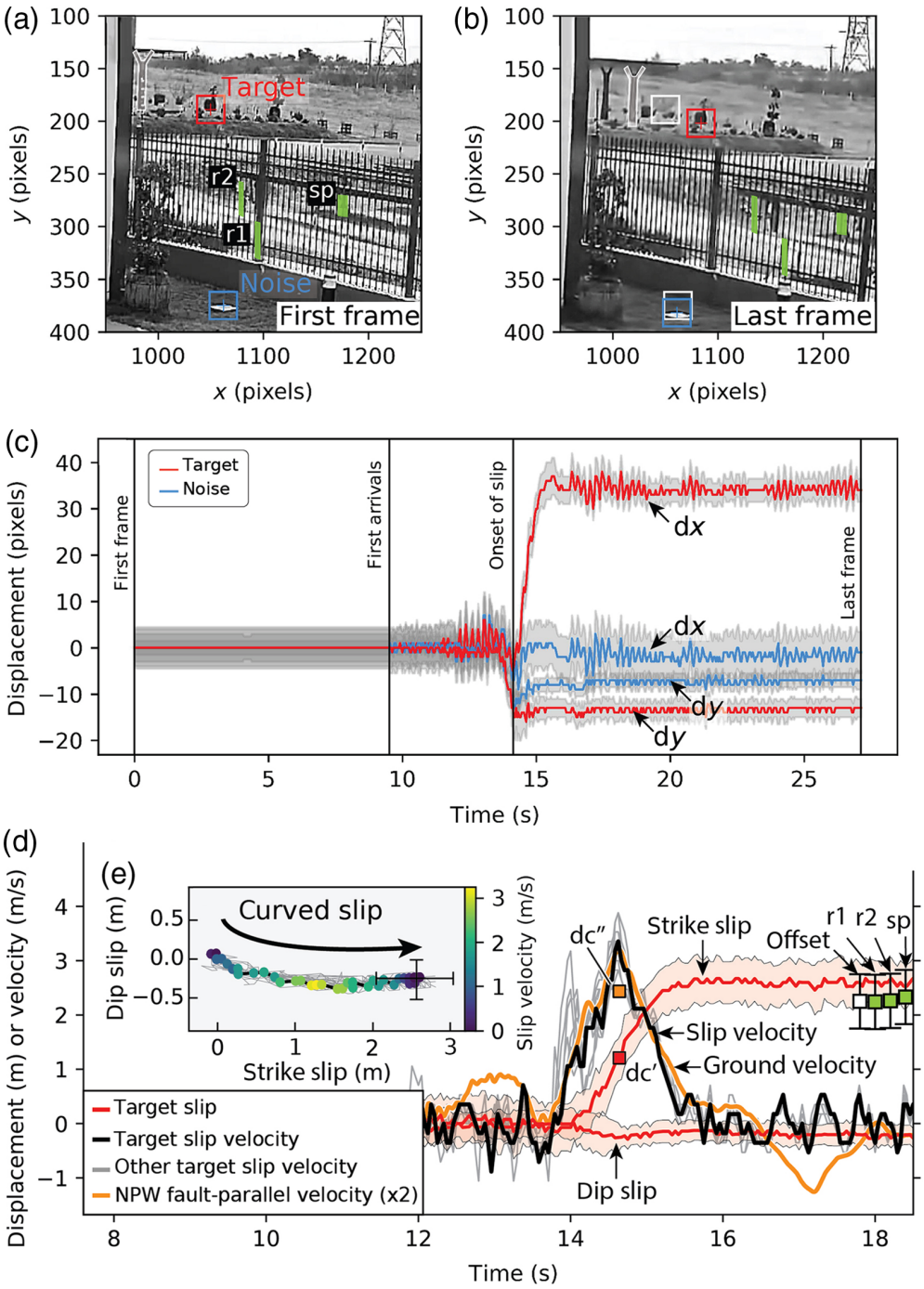

Figure 2. (a) The first frame and (b) the last frame of the CCTV video. The red box labeled "target" shows the 26-pixel window used to track displacements on the west (far) side of the Sagaing fault and on the east (near) side of the fault to correct for camera motion (blue box labeled "noise"). White boxes show the original pixel location of the target and noise in the first frame of the CCTV video. The locations of roadside posts (r1, r2) and solar panel (sp) are shown. (c) Time series of pixel displacements as measured by pixel cross correlation of target (red) and noise (blue); *y* displacements are inverted such that positive *y* displacement represents positive vertical movement within the image. (d) Time series of fault slip (red) and horizontal slip velocity (black). Dip slip assumes that the Sagaing fault is vertical. Gray velocity curves show the results of additional targets for comparison. Fault parallel offset of the footpath is shown for comparison, as well as total slip measured for r1, r2, and sp (green squares). Amplitude of fault-parallel ground velocity at NPW (orange) is doubled to compare with slip velocity. Slip weakening distance derived from on-fault slip velocity (*dc′*) and off-fault ground velocity (*dc″*). (e) Curved fault-slip trajectory colored by slip velocity. Curvature occurs at the beginning of slip before slip reaches maximum velocity and slip < *dc′*. Dip slip assumes that the Sagaing fault is vertical.

Fig. 2d). The slight increase in fault-parallel displacement amplitude (from 2.2 to 2.5 m) with distance from the fault (0–35 m) aligns with previous field observations of on- and off-fault coseismic strain associated with other large strike-slip ruptures (Kearse *et al.*, 2018; Rockwell *et al.*, 2002).

Slip on Sagaing fault reaches a peak rate of 3.2 ± 1 m/s at 14.6 ± 0.1 s, exhibiting a slightly asymmetric slip velocity envelope characterized by a longer deceleration tail (0.8 s) relative to the initial acceleration phase (0.5 s). For comparison, slip velocities derived from tracking additional targets are also shown (gray velocity curves, Fig. 2d) and exhibit similarly shaped velocity envelopes. The coseismic slip trajectory of the Sagaing fault is dominated by right-lateral strike slip and contains a nonzero time-dependent component of vertical slip, resulting in slip curvature (Fig. 2e). The first meter of slip accumulation is oblique (maximum rake of 35°), containing a component of down-to-the-west motion across the fault. This corresponds to the initial 0.5 s of the rupture as slip velocity is increasing. The subsequent 1.5 m of slip is characterized by nearly pure strike slip, corresponding to the final 0.8 s of rupture as slip velocity decreases and fault slip is arrested.

Our analysis demonstrates that the net slip direction is approximately horizontal, consistent with strike-slip motion. However, because of the inherent nonuniqueness in transforming pixel displacements into real-world coordinates, the exact orientation of the net slip vector cannot be precisely resolved. Despite this limitation, the consistent curvature observed across multiple slip trajectories suggests that this feature is robust and is independent of the precise slip direction.

Discussion and Conclusions

This video record provides the first direct observations of seismic fault slip in a natural earthquake. The observed slip duration (rise time of 1.3 s) and high slip velocity (>3 m/s) offer clear evidence of pulse-like rupture propagation at the site. Although pulse-like rupture is commonly observed in large earthquakes (e.g., Melgar and Hayes, 2017), the mechanisms responsible for slip arrest remain debated. Proposed explanations include self-healing of slip governed by velocity-dependent friction (Heaton, 1990) or stopping phases generated either at fault strength barriers (Beroza and Mikumo, 1996), fault edges (Day, 1982), or within the fault damage zone (Huang and Ampuero, 2011). Stopping phases originating from the base of the fault are anticipated for elongated strike-slip ruptures that saturate the seismogenic width—conditions that are clearly met by the 2025 rupture of the Sagaing fault. Modeling of rupture dynamics may provide some insight on this, but this is beyond the scope of this article.

Previously, on-fault evidence for time-varying slip direction has come primarily from curved slickenlines observed on exhumed fault planes. Although suggestive of dynamic processes, such geological observations lack a direct temporal context, limiting their ability to resolve rupture dynamics. This study presents the first direct observation of curved fault slip, providing real-time validation that curved slickenlines can form during seismic rupture (Fig. 3). The geometry of the curved slip trajectory on the Sagaing fault is consistent with curved slickenlines observed in other large strike-slip ruptures, such as the 2016 M_w 7.8 Kaikōura earthquake, New Zealand (Kearse *et al.*, 2019). During rupture of the Kekerengu fault in 2016, slip was initially oblique and subsequently curved to become dominantly strike-slip, forming a curved slip trajectory that closely resembles that of the Sagaing fault in 2025.

A key result of our analysis is the observation that slip on the Sagaing fault curves rapidly during the acceleration phase but remains linear as slip decelerates (Fig. 2e), a relationship that was not resolvable using geological data alone. This type of dynamic behavior during slip onset is a feature observed across a suite of dynamic rupture simulations (Kaneko *et al.*, 2008; Kearse and Kaneko, 2020). These models suggest a mechanism for slip curvature that is controlled by the dynamic stresses within the cohesive zone of the rupture, which is dependent on the direction of rupture propagation. The curvature of slip on the Sagaing fault as the 2025 Myanmar earthquake rupture propagated southward past the CCTV camera is consistent with these models, which predict transient uplift of the side of the fault moving in the direction of rupture propagation (east side of the Sagaing fault moves south and up) relative to the other side of the fault.

Fault-parallel velocity pulses in near-fault strong-motion records have been used to estimate the slip-weakening distance (d_c) on the nearby fault plane during rupture (Fukuyama and Mikumo, 2007; Kaneko *et al.*, 2017; Kearse *et al.*, 2024). However, this approach lacks direct on-fault observations of slip velocity, which are needed to validate the methods, and to quantify the influence of off-fault free-surface effects. This study provides the first opportunity to compare on-fault slip velocity and off-fault ground velocity at a strong-motion station during the same earthquake rupture and to compare estimates of slip-weakening distances between the two. The strong-motion station NPW (Lai *et al.*, 2025) is located 2.7 km from the Sagaing fault and 130 km farther south along

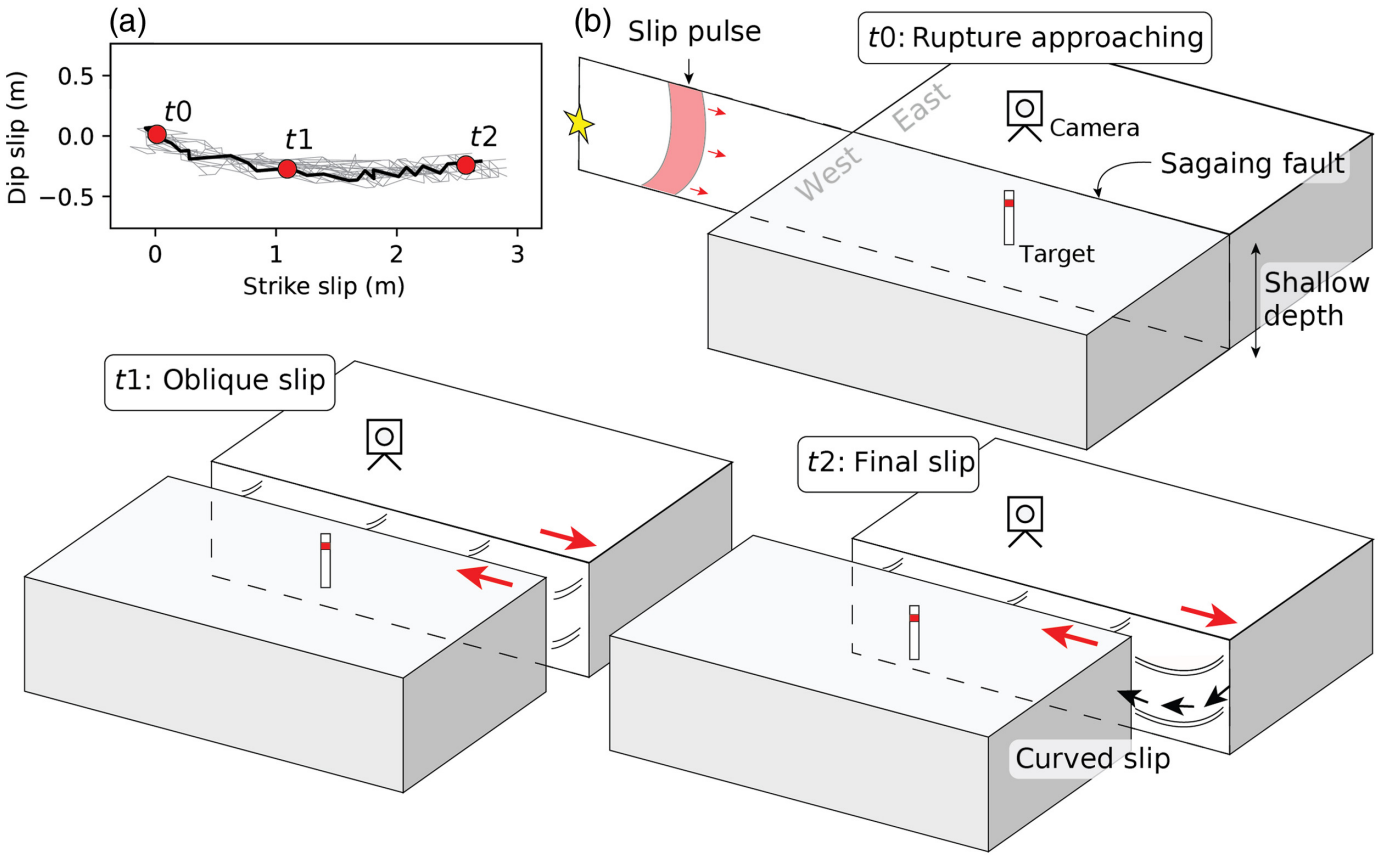

Figure 3. Schematic illustrating coseismic slip evolution on the Sagaing fault during the 2025 Myanmar earthquake. (a) Slip path of the Sagaing fault during the earthquake showing three key time intervals corresponding to snapshots shown in panel (b). (b) Schematic snapshots of slip evolution as the rupture front approaches the CCTV observation site from the north: at initial seismic-wave arrival (*t*0); during early slip acceleration with an oblique trajectory; including a down-to-the-west component (*t*1);, and after slip arrest (*t*2). Black curves on the fault plane depict the slip path that would be recorded by slickenlines.

strike from the location of this study (i.e., the rupture first arrived at the CCTV camera and later at NPW). Figure 2d displays the unfiltered fault-parallel component of ground velocity at NPW, but with its amplitude doubled to allow a more direct comparison with the on-fault slip velocity function. Both records show remarkable agreement, with similar amplitude, duration, and shape of the velocity function. This suggests that ground motions recorded at NPW likely reflect the off-fault signature of a pulse of slip on the nearby Sagaing fault during the 2025 Myanmar earthquake. This comparison supports the use of near-fault ground velocity records to constrain key rupture parameters—such as local rise time and peak slip velocity—to first order. These quantities are often difficult to uniquely resolve with conventional kinematic inversion techniques (Guatteri and Spudich, 2000; Konca Ozgun *et al.*, 2013). The slip-weakening distance estimated using the method of Fukuyama and Mikumo (2007) with the strong-motion data (dc'' = 2.4 m) is notably larger than that inferred from on-fault observations (dc' = 1.2 m; Fig. S7). This discrepancy likely reflects the added complexity in the ground velocity time series at NPW, including challenges in isolating direct fault-slip phases from secondary free-surface effects (e.g., Yao and Yang, 2025).

Overall, these observations establish a new benchmark for understanding dynamic rupture processes. They offer real-time confirmation that curved slickenlines can form during seismic slip, reinforce model-based interpretations of slip curvature governed by rupture dynamics, and validate near-fault ground-motion records as reliable proxies for on-fault slip behavior. Together these findings impose critical observational constraints on future rupture simulations and deepen our understanding of the physical mechanisms that control rapid fault slip during large earthquakes.

Data and Resources

Video used in this study is available at https://www.youtube.com/watch?v=77ubC4bcgRM (last accessed June 2025). Normalized cross correlation was performed using MATLAB's (www.mathworks.com/products/matlab, last accessed June 2025) built-in normxcorr2 function (R2024a, The MathWorks, Inc.). Coseismic displacements derived from Sentinel-2 images and presented in Figure 1a are available at doi: 10.5281/zenodo.15123647. The supplemental material for this article includes detailed descriptions of the video analysis and slip velocity data obtained from this study.

Declaration of Competing Interests

The authors acknowledge that there are no conflicts of interest recorded.

Acknowledgments

The authors thank Editor-in-Chief Keith Koper, Associate Editor Ruth Harris, Chelsea Scott, and anonymous reviewer for their comments, which improved this article. The authors thank Great Success Energy Co. Ltd for making the CCTV footage available and Nic Barth for insightful discussion and assistance with preliminary analysis. This work was supported by Japan Society for the Promotion of Science (JSPS) KAKENHI (21H05206, 23K03547) and Marsden Fund, Royal Society Te Aprangi (Project ID: GNS2002).

References

Barth, N. C., J. R. Kearse, T. A. Little, and R. J. Van Dissen (2024). Rupture direction of paleoearthquakes on the Alpine Fault, New Zealand, as recorded by curved slickenlines, *Geology* **52,** no. 12, 917–921.

Beroza, G. C., and T. Mikumo (1996). Short slip duration in dynamic rupture in the presence of heterogeneous fault properties, *J. Geophys. Res.* **101,** no. B10, 22,449–22,460.

Bouchon, M., N. Toksöz, H. Karabulut, M.-P. Bouin, M. Dietrich, M. Aktar, and M. Edie (2000). Seismic imaging of the 1999 Izmit (Turkey) rupture inferred from the near-fault recordings, *Geophys. Res. Lett.* **27,** no. 18, 3013–3016.

Cruz-Atienza, V. M., K. B. Olsen, and L. A. Dalguer (2009). Estimation of the breakdown slip from strong-motion seismograms: Insights from numerical experiments, *Bull. Seismol. Soc. Am.* **99,** no. 6, 3454–3469.

Day, S. M. (1982). Three-dimensional finite difference simulation of fault dynamics: Rectangular faults with fixed rupture velocity, *Bull. Seismol. Soc. Am.* **72,** no. 3, 705–727.

Fukuyama, E., and T. Mikumo (2007). Slip-weakening distance estimated at near-fault stations, *Geophys. Res. Lett.* **34,** no. 9, doi: 10.1029/2006GL029203.

Guatteri, M., and P. Spudich (2000). What can strong-motion data tell us about slip-weakening fault-friction laws? *Bull. Seismol. Soc. Am.* **90,** no. 1, 98–116.

Heaton, T. H. (1990). Evidence for and implications of self-healing pulses of slip in earthquake rupture, *Phys. Earth Planet. In.* **64,** no. 1, 1–20.

Huang, Y., and J.-P. Ampuero (2011). Pulse-like ruptures induced by low-velocity fault zones, *J. Geophys. Res.* **116,** no. B12, doi: 10.1029/2011JB008684.

Inoue, N., R. Yamaguchi, Y. Yagi, R. Okuwaki, B. Enescu, and T. Tadapansawut (2025). A multiple asymmetric bilateral rupture sequence derived from the peculiar tele-seismic P-waves of the 2025 Mandalay, Myanmar earthquake, *Seismica* **4,** no. 1, doi: 10.26443/seismica.v4i1.1691.

Kaneko, Y., E. Fukuyama, and I. J. Hamling (2017). Slip-weakening distance and energy budget inferred from near-fault ground deformation during the 2016 Mw 7. 8 Kaikōura earthquake, *Geophys. Res. Lett.* **44,** no. 10, 4765–4773.

Kaneko, Y., N. Lapusta, and J.-P. Ampuero (2008). Spectral element modeling of spontaneous earthquake rupture on rate and state faults: Effect of velocity-strengthening friction at shallow depths, *J. Geophys. Res.* **113,** no. B9, doi: 10.1029/2007JB005553.

Kearse, J., and Y. Kaneko (2020). On-fault geological fingerprint of earthquake rupture direction, *J. Geophys. Res.* **125,** no. 9, e2020JB019863, doi: 10.1029/2020JB019863.

Kearse, J., Y. Kaneko, T. Little, and R. Van Dissen (2019). Curved slickenlines preserve direction of rupture propagation, *Geology* **47,** no. 9, 838–842.

Kearse, J., Y. Kaneko, Y. Nozuka, C. Milliner, Y. J. Hsu, and J.-P. Avouac (2024). Strong asymmetry in near-fault ground velocity during an oblique strike-slip earthquake revealed by waveform particle motions and dynamic rupture simulations, *Seismica* **3,** no. 2, 1–12.

Kearse, J., T. A. Little, R. J. Van Dissen, P. M. Barnes, R. Langridge, J. Mountjoy, W. Ries, P. Villamor, K. J. Clark, A. Benson, *et al.* (2018). Onshore to offshore ground-surface and seabed rupture of the Jordan–Kekerengu–Needles fault network during the 2016 Mw 7.8 Kaikōura earthquake, New Zealand, *Bull. Seismol. Soc. Am.* **108,** no. 3B, 1573–1595.

Konca Ozgun, A., Y. Kaneko, N. Lapusta, and J.-P. Avouac (2013). Kinematic inversion of physically plausible earthquake source models obtained from dynamic rupture simulations, *Bull. Seismol. Soc. Am.* **103,** no. 5, 2621–2644.

Lai, S. T., K. M. Oo, Y. M. M. Htwe, T. Yi, H. H. Than, O. Than, Z. Min, T. M. Oo, P. M. Maung, D. Bindi, *et al.* (2025). Capacity building enables unique near-fault observations of the destructive 2025 M w 7.7 Myanmar earthquake, *Earth Syst. Sci. Data Discuss.* **2025,** 1–23.

Little, T. A., J. Kearse, Y. Kaneko, and R. Van Dissen (2025). Geometry of curved slickenlines as a function of rupture direction, asperity durability and coseismic roughening of fault surfaces, *J. Struct. Geol.* **190,** 105,291.

Melgar, D., and G. P. Hayes (2017). Systematic observations of the slip pulse properties of large earthquake ruptures, *Geophys. Res. Lett.* **44,** no. 19, 9691–9698.

Rockwell, T. K., S. Lindvall, T. Dawson, R. Langridge, W. Lettis, and Y. Klinger (2002). Lateral offsets on surveyed cultural features resulting from the 1999 Izmit and Duzce earthquakes, Turkey, *Bull. Seismol. Soc. Am.* **92,** no. 1, 79–94.

Spudich, P., M. Guatteri, K. Otsuki, and J. Minagawa (1998). Use of fault striations and dislocation models to infer tectonic shear stress during the 1995 Hyogo-ken Nanbu (Kobe) earthquake, *Bull. Seismol. Soc. Am.* **88,** no. 2, 413–427.

U.S. Geological Survey (USGS) (2025). M 7.7-2025 Mandalay, Burma (Myanmar) earthquake, available at https://earthquake.usgs.gov/earthquakes/eventpage/us7000pn9s/executive (last accessed June 2025).

Van Wyk De Vries, M. (2025). 2025 Myanmar earthquake displacement maps, *Zenodo*, doi: 10.5281/zenodo.15123647.

Vigny, C., A. Socquet, C. Rangin, N. Chamot-Rooke, M. Pubellier, M.-N. Bouin, G. Bertrand, and M. Becker (2003). Present-day crustal deformation around Sagaing fault, Myanmar, *J. Geophys. Res.* **108,** no. B11, doi: 10.1029/2002JB001999.

Witze, A. (2025). Deadly Myanmar earthquake was probably a rare rupture, scientists say, *Nature* **640,** no. 8058, 296–297.

Yao, S., and H. Yang (2025). Rupture phases reveal geometry-related rupture propagation in a natural earthquake, *Sci. Adv.* **11,** no. 4, eadq0154, doi: 10.1126/sciadv.adq0154.

Manuscript received 16 June 2025
Published online 18 July 2025

Supplementary material for *Curved fault slip captured by CCTV video during the 2025 Mw 7.7 Mandalay earthquake.*

Authors: Jesse Kearse[1] and Yoshihiro Kaneko[1]

[1]Graduate School of Science, Kyoto University, Japan.

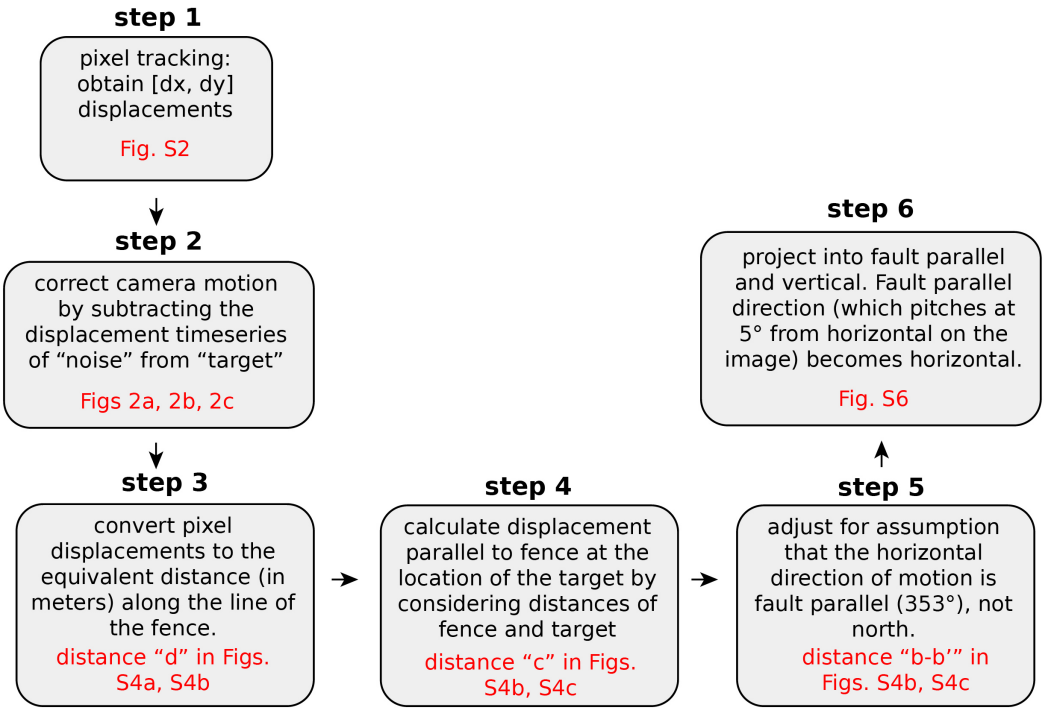

Figure S1: Flow chart outlining the steps involved with extracting fault slip data from the CCTV video file.

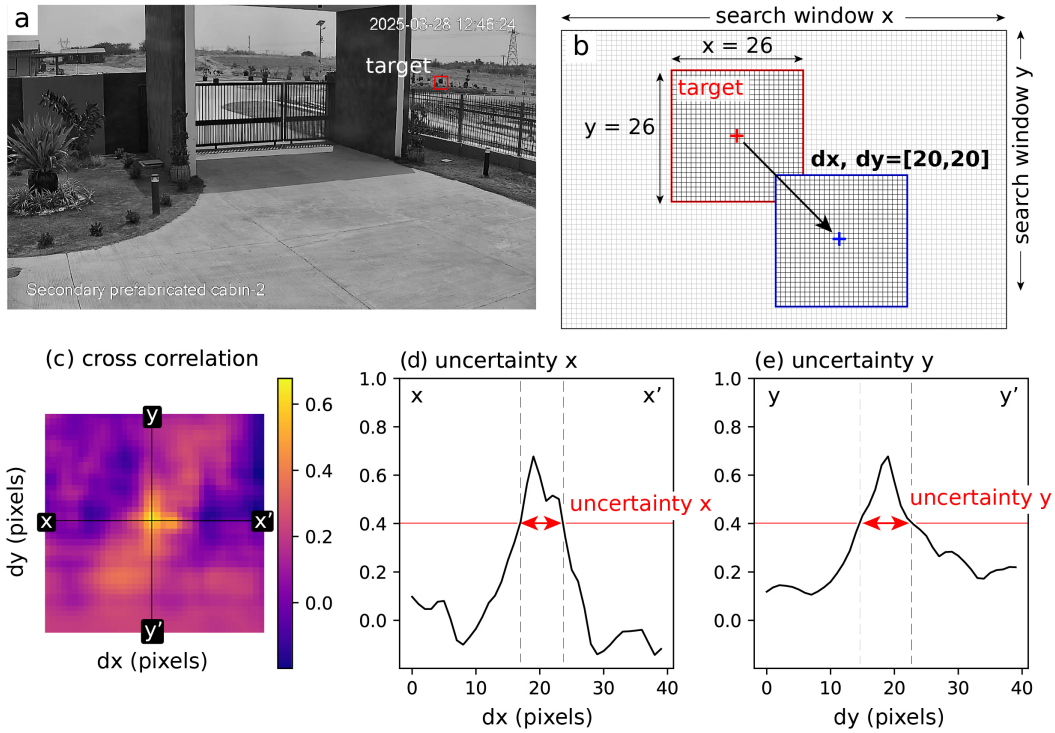

Figure S2: We use the Matlab function "normxcorr2" to perform normalized cross correlation between successive frames of the CCTV video file using the final frame as the reference. Displacements [dx, dy] at each iteration represent the maximum value of the cross correlation result. (a) Frame 1 showing the location of the target window. (b) Schematic showing the target window (red), the wider search window and the hypothetical dx, dy displacement result. (c) Cross correlation result at the location of the blue box in (b). x-x' and x-y' transects correspond to (d) and (e). Uncertainties are evaluated based on the sharpness of the correlation result in both dx (d) and dy (e) directions. pixel uncertainty bands are calculated based on the width of the cross correlation function where y = (peak value + mean value)/2 (red line = 0.4). Uncertainties are depicted in gray shading in Figs. 2c and 2d.

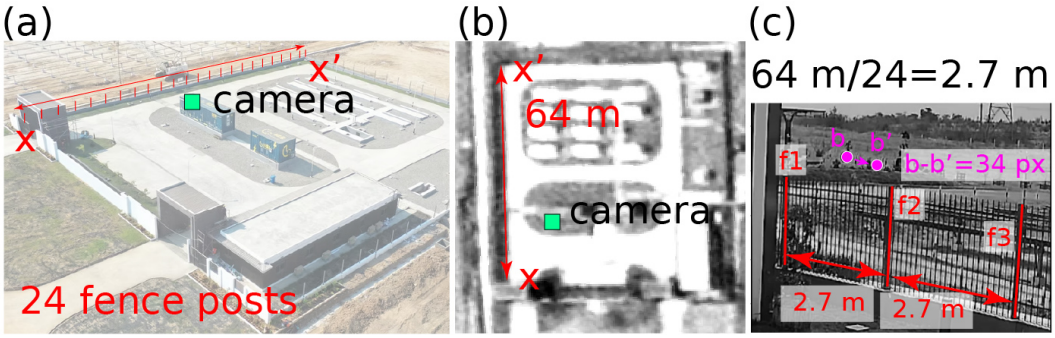

Figure S3: Distance between fence posts. (a) Oblique aerial photo showing the number of fence posts (24) along the length of edge of the enclosure. (b) Distance (64 m) of the length of the edge of the enclosure. (c) Distance in meters (2.7 m) between adjacent fence posts calculated by dividing the length of the fence by the number of fence posts. Locations of the target before b and after b' coseismic displacement are indicated.

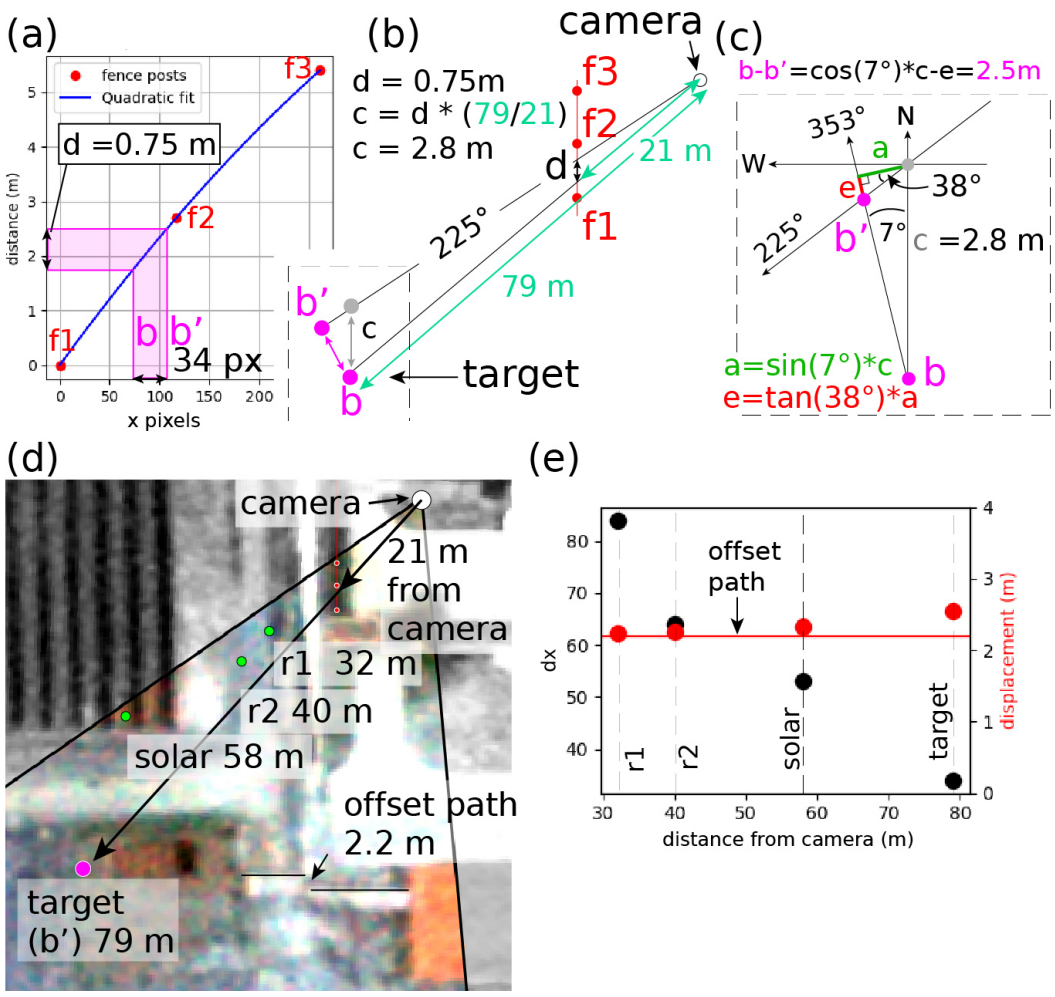

Figure S4: Scaling of pixel displacement of target b-b' (34 pixels) to real world displacement (2.55 m). (a) accounting for camera distortion. Quadratic function is used to calculate distance along the line of the fence. A distance of 0.75 m is calculated for pixel displacement of 34 between b and b'. (b) Calculation of displacement at the location of the target (79 m from the camera) along line c parallel to the fence (which is located 21 m from the camera). Distance of line c is equal to 2.8 m, which is derived by multiplying 0.75 m by the ratio of distances of the target and the fence (79 m/21 m). Distances and angles depicted in the diagram are not to scale. (c) We assume fault parallel displacement (353°) and no fault-normal displacement, and so convert line c to b-b'. (d) Planet satellite image showing locations of features 7 days after the event. (e) Illustration of parallax effect. Pixel displacements decrease as a function of distance from the camera (black points). Red points show the displacement in meters after the same procedure applied in (a)-(c). Horizontal red line shows the fault parallel offset of the path across the fault for comparison.

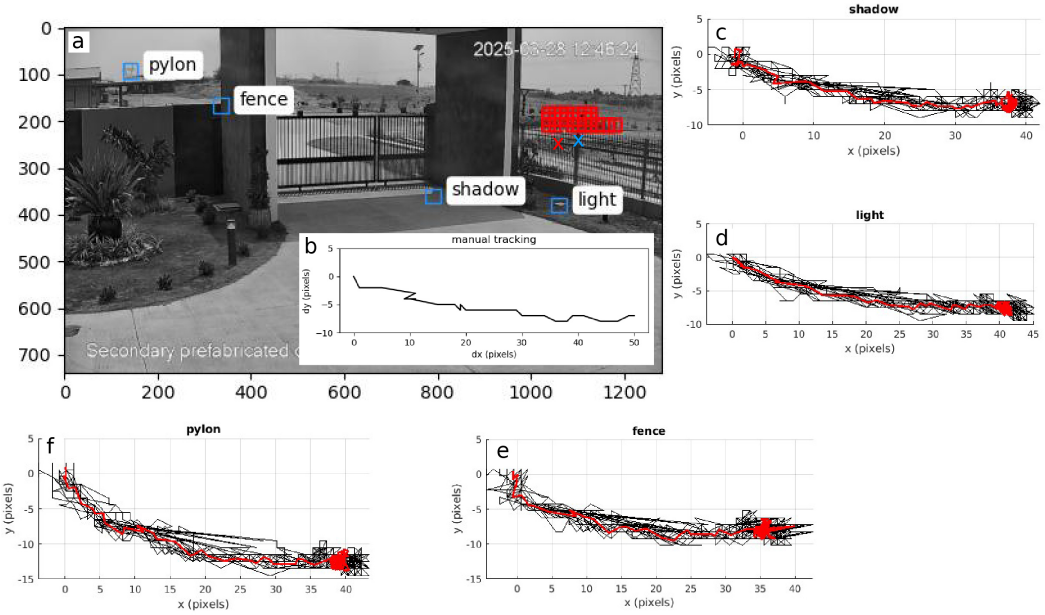

Figure S5: Agreement among different groups of target and noise sources. (a) Frame 1 of the video showing the location 22 targets used to track fault motion (overlapping red boxes) and 4 noise sources used to correct for camera motion (blue boxes). Pixel groupings must contain 2D structures in order to reliably track displacements in both x and y directions. Manually tracked target (corner of solar panel is shown as red x symbol), and manually tracked noise (fence shown as blue x symbol). Inset panel (b) shows the results of manual tracking. (c-f) Results of automatically tracked features using pixel cross correlation. black curves show the 22 target-noise displacement paths using noise corrections from shadow (c), light (d), fence (e), and pylon (f). Red curves show the mean. We choose the feature labeled as light to correct for camera motion, as it is closest to the targets. Despite the choice of noise or target, there a consistent trend of dynamic relative fault motion. Using the cross correlation of the pylon (located some 250 m from the camera) produces the same trend of relative fault motion, demonstrating that the trends observed are not introduced by vertical bulging within the surface rupture zone.

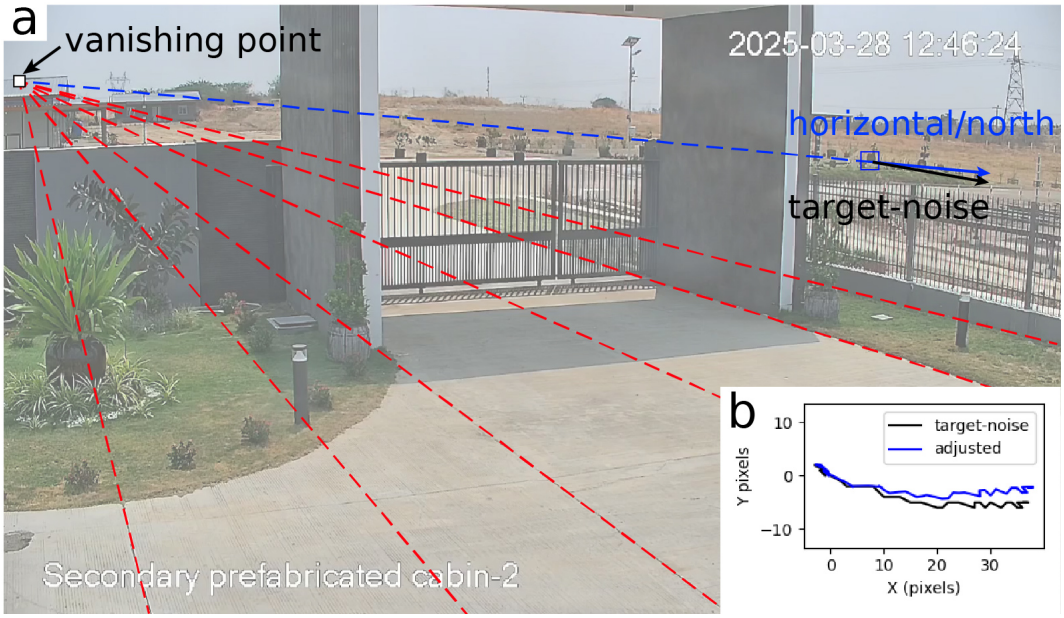

Figure S6: (a) Depiction of camera perspective effects and the convergence of north-aligned features in the scene (red lines) at the vanishing point. Each red line is a projection of linear north-aligned features on the ground surface. The blue line shows north direction at the location of the target. The black arrow shows the net displacement of the target after correction for camera motion, thus demonstrates that relative ground displacement must have contained (1) a positive east component of horizontal displacement (i.e. clockwise of north), or (2) a component of negative vertical displacement (down relative to the camera). For the initial oblique direction of slip to have been produced by predominantly horizontal motion would require a significant component of fault-normal motion, and a shallow fault dip angle to accommodate the slip. For example, the observed displacement in y direction of the target at 82 m distance (−6 pixels) corresponds to an angular change of 0.8° assuming a typical camera focal length of 15 mm, requiring 35 m of horizontal motion to achieve the same vertical displacement of 0.5 m ($0.5/\tan(0.8°)$). We suggest it is more likely that the evolution of dx/dy displacement components observed is the result of a component of down-to-the-west dip slip, and predominantly fault-parallel displacement on a near-vertical fault surface, which is consistent with the kinematics of the Sagaing Fault. Considering steep but non-vertical fault dip angles such as 80° (e.g., USGS report) does not impact our results, as the vertical component of slip is dominant e.g. $\cos(10°) \approx 0.9833$. Further, the perspective effect of the camera renders east-west and north-south horizontal lines to intersect at a low angle of $<20°$ at the location of the target. The north south direction (blue dashed line) is therefore a fair representation of the fault parallel direction (353°), which would be only 1° different from north in the projection of the video. (b) Rotation of dx/dy displacements (black) into the fault-parallel direction (blue).

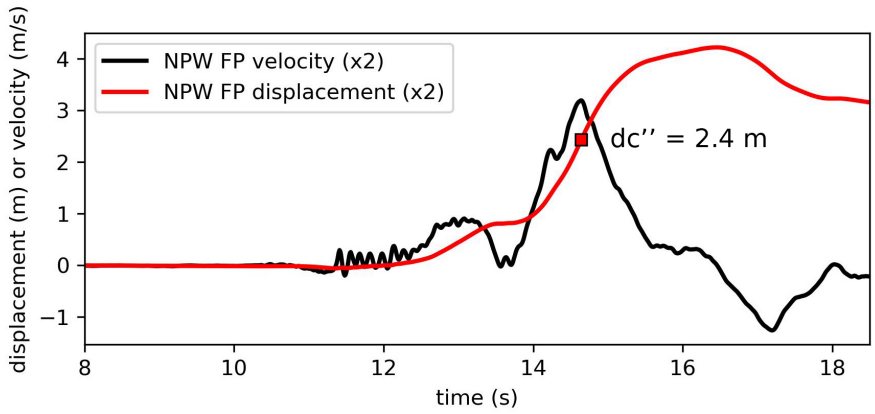

Figure S7: Fault parallel component of ground velocity and ground displacement at strong motion station NPW. The amplitude of both velocity and displacement waveforms has been doubled for consistency with Figure 2d. dc" measured from the displacement waveform at the time of peak ground velocity.